JOURNAL OF AIRCRAFT
Vol. 48, No. 1, January–February 2011

FENSAP-ICE-Unsteady: Unified In-Flight Icing Simulation Methodology for Aircraft, Rotorcraft, and Jet Engines

Cristhian N. Aliaga,* Martin S. Aubé,† and Guido S. Baruzzi‡
Newmerical Technologies International, Montreal, Quebec H3A 2M7, Canada
and
Wagdi G. Habashi§
McGill University, Montreal, Quebec H3A 2S6, Canada

DOI: 10.2514/1.C000327

In-flight ice accretion, even though driven by a steady flow airstream, is an inherently unsteady phenomenon. It is, however, completely ignored in icing simulation codes (one-shot) or, at best approximated via quasi-steady modeling (multishot). The final ice shapes thus depend on the length of the total accretion time (one-shot), or of the arbitrarily prescribed time intervals (multishot), during which the impact of ice growth on both airflow and water impingement is ignored. Such a longstanding heuristic approximation is removed in this paper by coupling in time the dilute two-phase flow (air and water droplets flow) with ice accretion, and is implemented in a new code, FENSAP-ICE-Unsteady. The two-phase flow is solved using the coupled Navier–Stokes and water concentration equations, and the water film characteristics and ice shapes are obtained from laws of conservation of mass and energy within the thin film layer. To continually update the geometry of the iced surface in time, arbitrary Lagrangian–Eulerian terms are added to all governing equations to account for mesh movement in the case of stationary components. In the case of rotating/stationary interacting components, a dynamically stitched grid is used. The numerical results clearly show that unsteady modeling improves the accuracy of both rime and glaze ice shape prediction, compared with the traditional quasi-steady approach with frozen solutions. The unsteady model is shown to open the door for a unified approach to icing on fixed wings, on helicopters with blades/rotors/fuselage systems. Problems of current concern in the icing community such as the ingestion of ice crystals at high altitude become tractable with the new formulation.

Nomenclature

C_D	=	droplet drag coefficient
c_p	=	specific heat
D_p	=	droplet diameter
$\mathbf{g}$	=	gravity vector
h	=	water film height
L	=	latent heat
$\dot{m}$	=	mass flow rate
p	=	pressure
Q	=	heat flux
Re	=	Reynolds number
T	=	temperature
t	=	time
U, V	=	velocity
$\mathbf{x}$	=	spatial coordinates
α	=	volume fraction
β	=	droplet collection efficiency
ρ	=	density
μ	=	kinematic viscosity
σ	=	Boltzmann constant
$\boldsymbol{\tau}$	=	shear stress vector, or pseudotime

Subscripts:

g	=	gas or air
p	=	particle or droplet
w	=	water
f	=	liquid water film
∞	=	far-field or reference

I. Introduction

IN-FLIGHT icing simulation codes in wide use by industry, such as LEWICE [1], ONERA [2] and FENSAP-ICE [3], combine 2-D or 3-D inviscid or viscous steady airflow analysis with a Lagrangian or Eulerian approach for water droplet dynamics, and the Messinger thermodynamic model for ice accretion. Despite the fact that ice accretion is a genuinely unsteady phenomenon, these icing codes use a quasi-steady approach in which the impact of ice growth on both flow and droplet fields is neglected during heuristically prescribed time intervals. During each of these time intervals, the airflow and water impingement are not recalculated, neither is surface roughness, but ice is continuously accreted driven by flow, impingement, and roughness values derived at a much earlier time. This is known as multishot ice accretion, leading to final ice shapes that are strongly dependent on the number of time steps (snapshots) taken. Empiricism and experience play an important role in getting it right:, i.e., how to space these shots in time to numerically duplicate ice shapes that are experimentally measured [4]. It has been recognized for years that such an approach is far from general and that a truly unsteady approach must be taken [5–9].

The need for multishots is confirmed by the fact that different features can be observed on the ice shape if multiple layers of ice are grown using a periodic update of the airflow and impingement. For instance, a one-shot ice accretion predicts a larger ice thickness on the suction side of a wing, as one neglects the growing shadowing effects of the accumulated ice in time. For glaze icing, among the various characteristics that can be compared with experiments, horns

Received 24 February 2010; revision received 1 September 2010; accepted for publication 1 September 2010.

*Chief Consulting Services, 680 Sherbrooke Street W.
†Vice-President Operations, 680 Sherbrooke Street W.
‡Director Product Development, 680 Sherbrooke Street W.
§Professor, Department of Mechanical Engineering and Director CFD Lab, 688 Sherbrooke Street W. Fellow AIAA.

location and angle are probably the most difficult to capture. Their growth being unsteady by nature, they may not be properly modeled through one-shot ice accretion. Therefore, a large number of simulations for very small time spans would be necessary to obtain satisfactory results, requiring a complete remeshing of the 3-D computational domain for each simulation. An alternative would be to use reduced order modeling such as Panel methods (inviscid incompressible) for flow and empirical roughness that varies in time [1] to allow a quick refresh of the flow features, at the sacrifice of accuracy and fidelity due to corrective formulations and correlations that make this approach vulnerable to limiting cases such as flow separation caused by ice horns, and ice accretion at wing tips. These two alternatives are costly, impractical or not suitable for long-time ice accretions on complex and arbitrary geometries.

The above part of the introduction concerned itself with the need to upgrade models of in-flight icing on stationary components. One must in addition consider that no icing code can at the present time calculate water impingement or ice accretion in a totally 3-D unsteady manner on rotating components adjacent to stationary ones, such as in the case of turboprops, rotorcraft or in jet engines. Yet, not only does industry need such capabilities in the design and certification phases, as testing is quite limiting, but recent safety problems caused by the ingestion of ice crystals by engines at cruise altitudes has industry clamoring for experimental and numerical tools to understand, and, it is hoped, remedy the problem [10].

The current paper presents a 3-D in-flight icing unsteady formulation that unifies the approach for analyzing aircraft, rotorcraft and jet engines. The formulation removes the quasi-steady assumption by ensuring time-accurate results, while at the same time dispensing with remeshing. The approach is based on a multiphase system of partial differential equations (PDEs) that couples, in a fully unsteady manner, a two-phase flow (air + droplets) to the icing model. The film height and temperature, and the growing ice shape, are solved in time from the conservation of mass and energy within the thin film layer.

To take into account surface growth and distortion due to ice without remeshing, Arbitrary Lagrangian-Eulerian (ALE) terms are added to the set of governing equations, and an interface reconstruction algorithm is implemented to smooth the iced surface with respect to mesh spacing, grid curvature and orthogonality criteria. In the case of rotating components, a mesh-stitching algorithm is implemented, guaranteeing conservation of quantities.

In this paper, the unsteady icing model is validated for rime and glaze icing conditions on wings and is compared for ice form, thickness distribution, and horn angles against NASA-Icing Research Tunnel experimental measurements. The dearth of open literature experimental results for three-dimensional geometries, the closely guarded proprietary ones, and the almost complete absence of experimental results for rotating components in icing conditions, reverses the traditional relationship of computational fluid dynamics (CFD) vis-à-vis experiments, by curiously setting CFD algorithmic innovations of in-flight icing as the driver for experimentation. The methodology is then applied and validated for the prediction of unsteady impingement zones of rotating components, such as for the interaction of a model helicopter rotor and fuselage.

II. Unsteady Two-Phase Model: Governing Equations and Solution Methodology

Conservation of mass and momentum can be defined as follows for an Eulerian formulation of multiphase flows, with moving grids, with Eq. system (1) for air and Eq. system (2) for water droplets concentration:

$$\frac{d(\alpha_g p_g)}{dt} - \frac{dx_k}{dt}\frac{\partial(\alpha_g p_g)}{\partial x_k} + \frac{\partial(\alpha_g p_g V_{g,i})}{\partial x_i} = 0$$
$$\frac{d(\alpha_g p_g V_{g,i})}{dt} - \frac{dx_k}{dt}\frac{\partial(\alpha_g p_g V_{g,i})}{\partial x_k} + \frac{\partial(\alpha_g p_g V_{g,i} V_{g,k})}{\partial x_k} = -\alpha_g \overset{\mathrm{r}}{\nabla}_{p_g} + \overset{\mathrm{r}}{\nabla}\cdot(\alpha_g \overset{\mathrm{r}}{\boldsymbol{\tau}}_g) + \alpha_g p_g \overset{\mathrm{r}}{g} - K \quad (1)$$

$$\frac{d(\alpha_p p_p)}{dt} - \frac{dx_k}{dt}\frac{\partial(\alpha_p p_p)}{\partial x_k} + \frac{\partial(\alpha_p p_p V_{p,i})}{\partial x_i} = 0$$
$$\frac{d(\alpha_p p_p V_{p,i})}{dt} - \frac{dx_k}{dt}\frac{\partial(\alpha_p p_p V_{p,i})}{\partial x_k} + \frac{\partial(\alpha_p p_p V_{p,i} V_{p,k})}{\partial x_k} = -\alpha_p p_p\left(1 - \frac{p_g}{p_p}\right)\overset{\mathrm{r}}{\mathbf{g}} + K \quad (2)$$

with

$$K = \frac{3}{4}\alpha_g \alpha_p C_D \frac{\mu_g}{D_p^2} Re_p (V_{g,i} - V_{p,i})$$

The two systems of equations express the impact of water droplets on air and that of air on the droplets. The time derivative of grid coordinates accounts for mesh displacement in an ALE formulation.

Under in-flight icing conditions, the ratio between LWC of droplets and air mass is usually of the order of 10^{-3}, leading to a droplet volume fraction α_p of the order of 10^{-6}. The air volume fraction α_g can thus be considered constant and equal to 1. The air-droplet flow is then viewed as a dilute gas-particle system, where only the effects of air on droplets are considered and where water droplets are treated as spherical particles, without coalescence, deformation, collision, splashing, or breakup. The resulting simplified equations for air, neglecting gravity, are:

$$\frac{d(p_g)}{dt} - \frac{dx_k}{dt}\frac{\partial(p_g)}{\partial x_k} + \frac{\partial(p_g V_{g,i})}{\partial x_i} = 0$$
$$\frac{d(p_g V_{g,i})}{dt} - \frac{dx_k}{dt}\frac{\partial(p_g V_{g,i})}{\partial x_k} + \frac{\partial(p_g V_{g,i} V_{g,k})}{\partial x_k} = \overset{\mathrm{r}}{\nabla}_{p_g} + \overset{\mathrm{r}}{\nabla}\cdot(\overset{\mathrm{r}}{\boldsymbol{\tau}}_g) \quad (3)$$

and for water:

$$\frac{d(\alpha_p)}{dt} - \frac{dx_k}{dt}\frac{\partial(\alpha_p)}{\partial x_k} + \frac{\partial(\alpha_p V_{p,i})}{\partial x_i} = 0$$
$$\frac{d(V_{p,i})}{dt} - \frac{dx_k}{dt}\frac{\partial(V_{p,i})}{\partial x_k} + V_{p,k}\frac{\partial(V_{p,i})}{\partial x_k} = \frac{3}{4}\frac{1}{p_p} C_D \frac{\mu_g}{D_p^2} Re_p (V_{g,i} - V_{p,i}) \quad (4)$$

Unsteady ice accretion is simulated by coupling, at each time step, the air and water solvers to the Messinger model for rime ice. Under rime icing conditions, when droplets hit and freeze instantaneously, the inviscid equations and a condition of constant total enthalpy can prove sufficient. For glaze icing conditions, however, when droplets remain liquid, run along and freeze at other than the impact points, the viscous turbulent equations must be solved along with the energy equation for computing the necessary shear stresses and heat fluxes on walls.

To solve the equations, spatial discretization is by a finite element method using equal interpolation for all variables. The governing equations are linearized by a Newton method and the solution advanced in time by an implicit dual time stepping scheme [11] that improves the stability of the linear matrix system for large time steps, and reduces the total computational time for unsteady calculations. The resulting linear system is second-order in both space and time, and is solved iteratively using a generalized minimum residual (GMRES) algorithm. The CFD (FENSAP) and impingement (DROP3D) modules of the FENSAP-ICE system have been extensively validated for external and internal aerodynamics and for water impingement, such as in [3,12].

III. Calculating Ice Accretion

A. Rime Icing

At very low temperatures, most of the water droplets impinging on a solid surface will freeze upon impact. In this particular case, ice accretion is mainly represented by a simple mass balance between droplet impingement and ice accretion

$$U_\infty(\mathrm{LWC}_\infty)\beta = U_\infty \rho_{\mathrm{ice}} \dot{m}_{\mathrm{ice}} \qquad \dot{m}_{\mathrm{ice}} = \frac{\mathrm{LWC}_\infty}{\rho_{\mathrm{ice}}}\beta \tag{5}$$

B. Glaze Icing

Glaze icing regions are represented by a thin film of water that develops above the exposed iced surface across which a linear velocity profile can be assumed

$$\bar{u}_f = \frac{y}{\mu_{\mathrm{wall}}} \vec{\tau}_{\mathrm{wall}}(\vec{x}, y) \tag{6}$$

where $x = (x_1, x_2)$ is the curvilinear coordinate system on the surface, and y is the normal direction. The conservation of mass within the thin film of water can be expressed by averaging along the normal direction:

$$\int_S \rho_w \left[\frac{\partial h_f}{\partial t} + \mathrm{div}(\bar{u}_f h_f)\right] \vec{dx} = \int_S (U_\infty \mathrm{LWC}_\infty \beta - \dot{m}_{\mathrm{evap}} - \dot{m}_{\mathrm{ice}})\, \vec{dx} \tag{7}$$

The source terms correspond, respectively, to the mass flow rate of droplets impingement, water evaporation, and ice accretion. The conservation of energy within the thin film, accounting for water droplet impingement, evaporation, ice accretion, and air convection is:

$$\begin{aligned}
&\int_S p_w \left[\frac{\partial h_f c_{p,w} T_{\mathrm{equi}}}{\partial t} + \mathrm{div}(\bar{u}_f h_f c_{p,w} T_{\mathrm{equi}})\right] \vec{dx} \\
&= \int_S U_\infty \mathrm{LWC}_\infty \beta \left[c_{p,w}(T_{d,\infty} - T_c) + \frac{\|\bar{u}_d\|^2}{2}\right] \vec{dx} \\
&- \frac{1}{2}\int_S [L_{\mathrm{evap}}(T_c) + L_{\mathrm{sub}}(T_c)]\dot{m}_{\mathrm{evap}}\, \vec{dx} \\
&+ \int_S [L_{\mathrm{fus}}(T_c) - c_{p,\mathrm{ice}}(T_{\mathrm{equi}} - T_c)]\dot{m}_{\mathrm{ice}}\, \vec{dx} \\
&+ \int_S Q_{\mathrm{conv}}\, \vec{dx} + \int_S \sigma\varepsilon[T_\infty^4 - T_{\mathrm{equi}}^4]\, \vec{dx} \\
&+ \int_S c_{p,w} T_c [U_\infty \mathrm{LWC}_\infty \beta - \dot{m}_{\mathrm{evap}} - \dot{m}_{\mathrm{ice}}]\, \vec{dx}
\end{aligned} \tag{8}$$

The last integral on the right-hand side is a corrective one for change of temperature units.

Mass and energy equations are discretized using a finite volume Roe scheme and require, at each time step, the convective heat fluxes, shear stresses, and collection efficiencies from the two-phase model. After solution, surface displacement vectors Δh_{ice} are computed from the mass rate of ice accretion

$$\bar{v}_{\mathrm{ice}} = \frac{\dot{m}_{\mathrm{ice}}}{\rho_{\mathrm{ice}}}\mathbf{n} = \frac{dh_{\mathrm{ice}}}{dt}\mathbf{n} \approx \frac{\Delta h_{\mathrm{ice}}}{\Delta t}\mathbf{n} \qquad \Delta h_{\mathrm{ice}}\mathbf{n} = \Delta t \frac{\dot{m}_{\mathrm{ice}}}{\rho_{\mathrm{ice}}}\mathbf{n} \tag{9}$$

and imposed as boundary conditions to the two-phase and mesh deformation models.

IV. Mesh Deformation-Movement and Mesh Stitching

The section will describe two algorithms:

1 For stationary components: an algorithm to deform and move the mesh at each time step of the unsteady ice accretion process around a stationary object such as an aircraft wing.

2 For moving components: a stitching algorithm to continuously create an appropriate mesh around a rotating object such as a helicopter rotor.

A. Mesh Deformation-Movement for Icing in a Stationary Context (Aircraft Wings)

The most cost-effective mesh movement methods are based on a Laplacian operator, such as the spring or elastic methods [13]. Remeshing [14] or unsteady mesh adaptation [15], while more robust, are expensive and not needed as the ice surface experiences very small deformations at each time step of a truly unsteady process.

The Laplacian operator proposed by Lepage and Habashi [16] solves for nodal displacements in an uncoupled fashion, using the nodal wall distance as a stiffness factor:

$$\nabla \cdot (k\nabla(\Delta x)) = 0 \qquad k(x, y, z) = 1 + \frac{1}{d_{\mathrm{tol}} + d(x, y, z)} \tag{10}$$

where d is the distance from a node to the wall, and d_{tol} represents a small tolerance. The stiffness factor k is a monotonically decaying function that preserves the shape and quality of the tight grid near the wall, and affects nodal displacements of the coarse grid far from the wall. To solve this linear system two Dirichlet conditions are required: a prescribed displacement on the interface and a zero displacement in the far field.

As ice accretes in the normal direction to the surface, the distance between wall nodes will either stretch (positive local curvature), or contract (negative local curvature), leading to coarse surface meshing or ultimately to negative volume elements. Elaborate interface smoothing techniques are devised to judiciously and continuously repartition iced surface nodes with respect to mesh spacing, grid curvature and orthogonality criteria while preserving the ice layer [12].

B. Mesh Stitching for Icing in Rotating/Stationary Contexts (Propellers and Rotors)

The unsteady icing model is applied to such flows by considering two grid domains: the first being fixed around the stationary object (for example the fuselage), and the second rotating with the blades (propellers, rotors, etc.); the domains being separated by a small gap in space. Flow and droplet calculations are performed in an absolute frame of reference, with the gap region being constantly remeshed or stitched with tetrahedral elements. This method ensures full mass conservation without any special treatment and is easily implemented in a finite element context, as opposed to Chimera grids, or overset meshes, which require interpolation of flow variables from one grid to another, and can thus lead to conservation issues.

The stitching algorithm implemented here is based on a simplified advancing front technique where the gap is filled incrementally by only adding tetrahedral elements. The algorithm starts with an initial advancing front that generates a transitional mesh by joining surrounding surface triangles to nodes on the opposite surface. The advancing front is constantly displaced as new elements are added to the grid. This incremental procedure is repeated until the gap is completely filled with elements. Such remeshing has proven to be sufficiently robust to stitch surfaces of similar shape and element density.

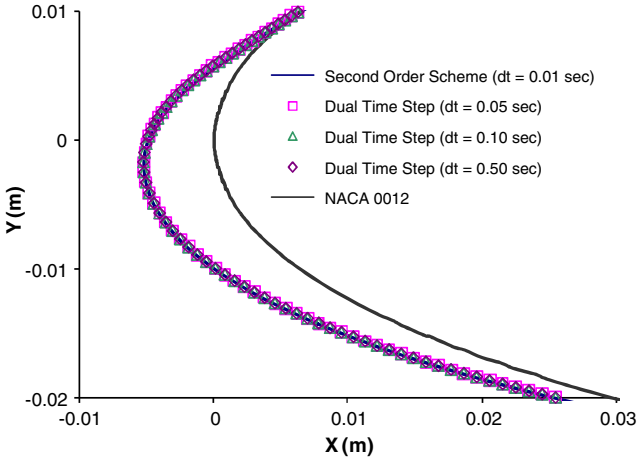

Fig. 1 Ice shapes after 2 min of rime ice accretion.

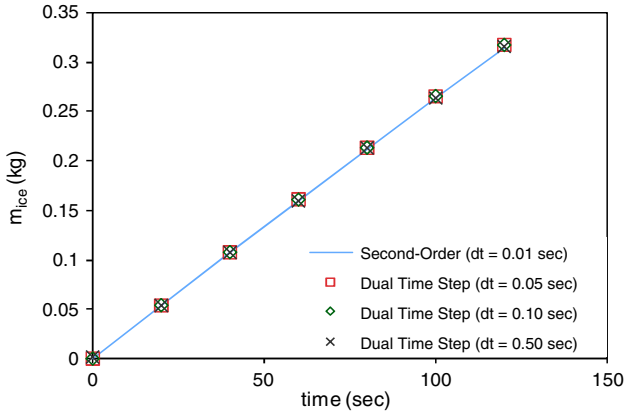

Fig. 2 Evolution of mass of ice within 2 min of rime ice accretion.

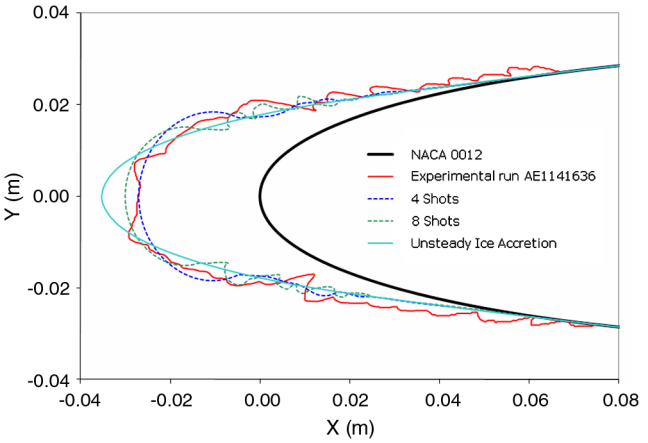

Fig. 3 4.1-min rime ice accretion on NACA0012 wing.

V. Solution Accuracy via Dual-time Stepping

The impact of the dual time stepping is examined by using different time steps for second-order accurate and dual time stepping runs. All simulations are run without smoothing techniques, to examine only the sensitivity of the final ice shapes to the physical time step. In this case, the maximum physical time step that allowed convergence of the linear equations using the second-order Gear scheme was 0.01 s. Therefore, the tested physical time steps of the dual time stepping simulations are then 0.05, 0.1, and 0.5 s to achieve a significant speedup.

After 2 min of ice accretion, all numerical results predict the same ice shape as depicted in Fig. 1. The consistency between second-order and dual time stepping is reconfirmed by examining the evolution in time of the mass of ice captured. From Fig. 2, the mass of ice captured by the NACA 0012 using a second-order formulation or dual time stepping formulation is the same, the maximum difference between dual time stepping schemes and the time-accurate scheme being 0.9%. This suggests that, within the range of 0.01 and 0.5 s, the multiphase icing model predicts consistent results regardless of the use of a second-order scheme or dual time stepping.

The advantage of using the dual time stepping scheme with large time steps is evident from Table 1. By using dual time stepping with a physical time step of 0.5 s, it becomes possible to decrease the total computational time 38-fold with respect to the maximum time step allowed by the time-accurate scheme (0.67 h vs 25.54 h), without compromising numerical accuracy.

VI. Aircraft Applications: Unsteady Ice Accretion on Stationary Components

A. Rime Ice Accretion

The proposed icing model is compared with experimental results from the NASA Glenn Icing Research Tunnel (IRT). In this case, a pure rime icing condition is simulated (Table 2) on a section of a NACA0012 wing. Rime ice accretion is computed using a constant ice density and a time step of 0.5 s. Total time of accretion is 4.1 min.

Figure 3 shows that the ice shape prediction of FENSAP-ICE-Unsteady (light bleu curve) compares well with experiments. A small discrepancy is observed close to the leading edge and may be explained by the representation in the calculation of the entire cloud droplet spectrum by only its median volume diameter droplet. This ignores the substantial mass of very large droplets with high collision efficiency near the stagnation line. The figure also contrasts the unsteady result to two multishot results obtained by FENSAP-ICE. These multishots have a uniform time span. The unsteady simulation removes the artificial shadow zones created by the multishot simulations.

B. Glaze Icing

The next calculations show the applicability of FENSAP-ICE-Unsteady in solving glaze icing. The NACA0012 grids are much finer for viscous turbulent flow calculations carried out using the Spalart–Allmaras one-equation turbulence model. The icing conditions examined are given in Tables 3 and 4. Total time of accretion is 2.9 min for Fig. 4 icing conditions, and 3.85 min for Fig. 5 icing conditions. In both cases, the physical time step is 0.05 s.

Discrepancy is observed between the unsteady simulated ice shapes and the experimental results. Regardless of the surface roughness magnitude, the upper and lower horn angles are not captured correctly. This suggests that the unsteady ice accretion model requires a time and space dependent surface roughness model to maintain horn angles.

Figure 6 shows that, as the glaze ice growth becomes significant and the horns begin to protrude substantially, due to the uneven and increasing curvature of the ice surface the ALE mesh displacement

Table 1 Computational time vs time integration

Scheme	Time step, s	Computational time, h
Second order	0.01	25.54
Dual-time step	0.05	6.45
Dual-time step	0.1	3.28
Dual-time step	0.5	0.67

Table 2 4.1-minute ambient conditions for rime ice simulation

T_∞	−29.37°C	MVD	51.04 μm
p_∞	100 kPa	LWC	2.58 g/m^3
V_∞	57.43 m/s	Mach	0.18
AoA	0°	ρ_{ice}	917 kg/m^3

Table 3 2.9-min ambient conditions for glaze ice simulation

T_∞	−13.4°C	MVD	50.33 μm
p_∞	100 kPa	LWC	2.24 g/m^3
V_∞	90.54 m/s	Mach	0.28
AoA	0°	Re	3.9×10^6

Table 4 3.85-min ambient conditions for glaze ice simulation

T_∞	−11.11°C	MVD	20 μm
p_∞	100 kPa	LWC	1 g/m^3
V_∞	102.8 m/s	Mach	0.317
AoA	3.8°	Re	4.4×10^6

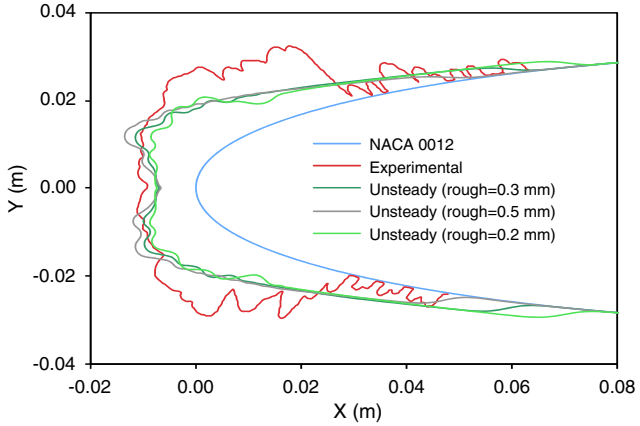

Fig. 4 2.9-min glaze ice accretion on NACA0012 wing.

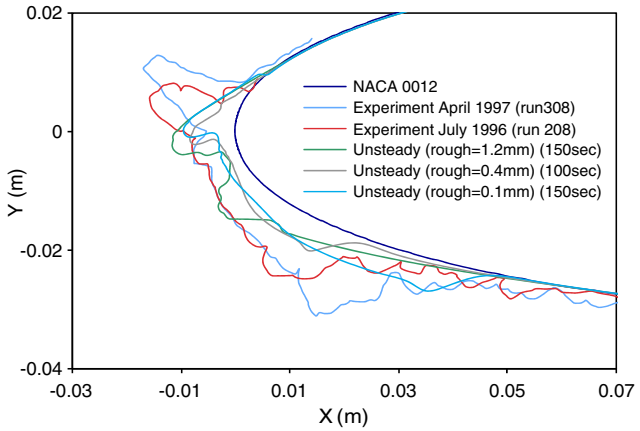

Fig. 5 3.85-min glaze ice accretion on NACA0012 wing.

algorithm increases the local element skewness. Remeshing should be performed before the elements become degenerate, but in this case the temporal continuity of the simulation would be broken. The remedy to this problem is still an area of intense investigation.

VII. Rotorcraft Applications: Unsteady Impingement on the Fuselage Caused by the Rotor

The selected model geometry, from Georgia Tech, consists of a two-bladed rotor interacting with a cylindrical fuselage. The blades have a NACA 0015 wing constant section of 86-mm chord (rectangular planform). The pitch angle is kept constant at 10 deg. The 0.457 m radius (R) rotor has tip path plane longitudinal and lateral flapping angles of, respectively, 4.06 and 2.03 deg. The shaft

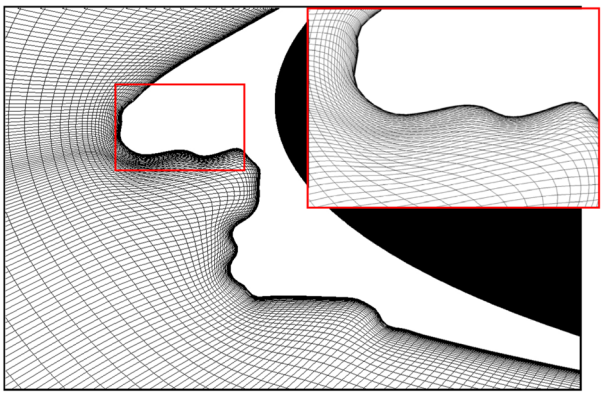

Fig. 6 Skewed elements after 150 s of Table 4 icing conditions.

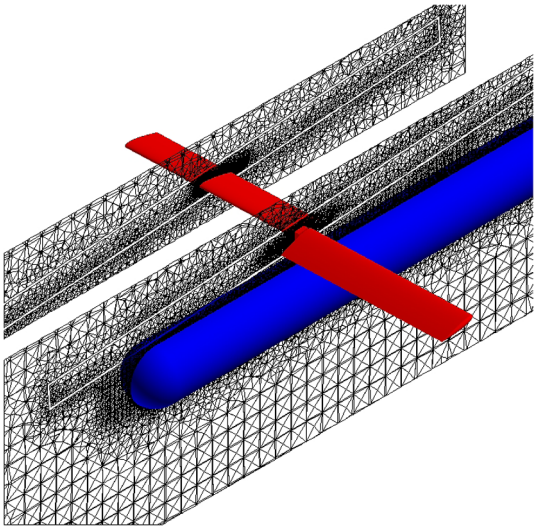

Fig. 7 Computational domain for two-blade rotor interacting with fuselage.

speed is constant at 2100 rpm, leading to an advance ratio (i.e., the ratio of the tunnel freestream velocity to the blade tip speed) of 0.1.

The test case and experimental data details are presented in [17–20]. Phase-averaged surface pressure coefficients were measured on the cylinder at four different stations, among which station 2 is located 289.81 mm upstream of the rotation center or at $X_b/R=$ 0.367, where X_b is measured from the airframe nose. Azimuth-resolved velocity measurements were also performed at different stations. In this work, results are compared 365.5 mm upstream of the rotation center and 14.346 mm above the cylinder airframe (or $X_b/R = 0.2$ and $Z_b/R = 0.178$, where Z is measured from the airframe centerline, positive upward).

A. Grid Stitching and Unsteady Flows

Because of the complexity of the problem and the unavailability of experimental data for impingement or ice accretion, it was decided to use an Euler model rather than turbulent Navier–Stokes. The unstructured grid is composed of two volumes surrounding the two geometrical components, the static fuselage (blue) and the moving rotor (red), separated by a small gap in space, as shown in Fig. 7. The gap spacing is set to approximately the edge length of the triangles on the gap surfaces. The number of grid points (2.2 million) and elements (7.4 million tetrahedra, pyramids, and prisms) are kept relatively small to minimize solution time.

Figure 8 compares periodic pressure coefficient variations measured at station 2 with numerical predictions, showing significant pressure increase due to the passage of the two rotor blades. The unsteady pressure coefficient is defined as the difference

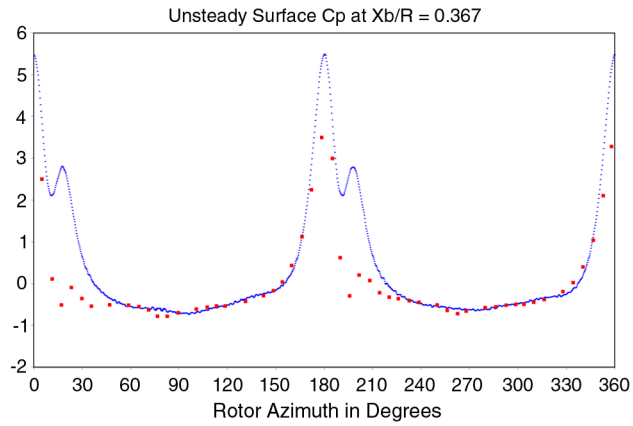

Fig. 8 Pressure coefficient at station 2 (continuous dotted line= numerical; square points = experiment).

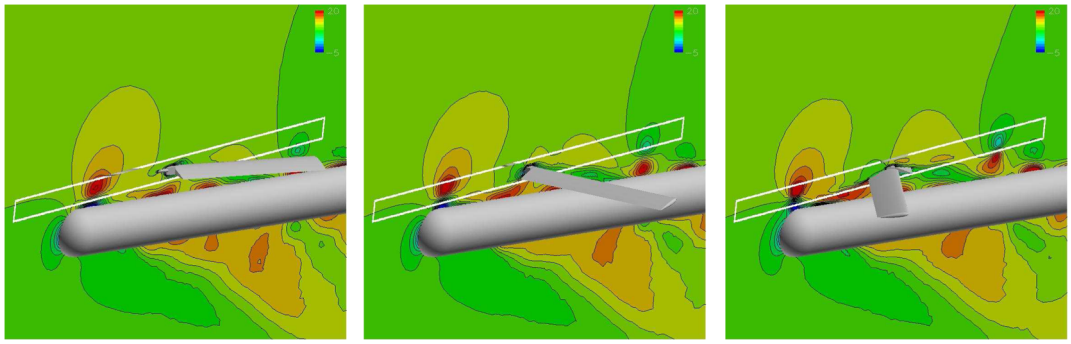

Fig. 9 Axial velocity on the $Y = 0$ cutting plane at three snapshots in time.

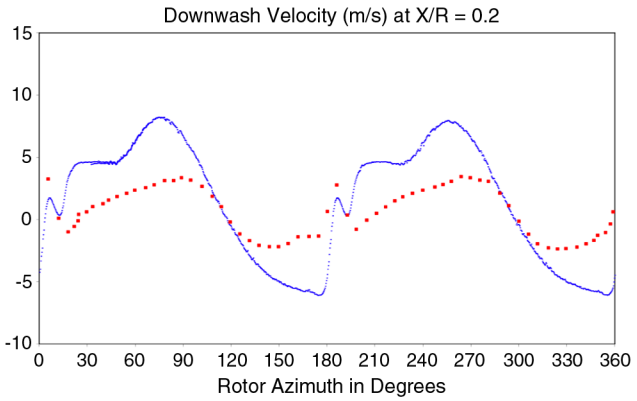

Fig. 10 Downwash velocity at $X/R = 0.2$ (continuous dotted line = numerical; square points = experiment).

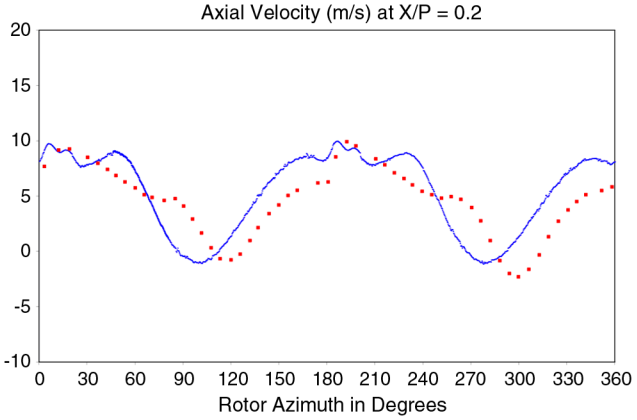

Fig. 11 Axial velocity at $X/R = 0.2$ (continuous dotted line = numerical; square points = experiment).

between the instantaneous pressure and the local mean static pressure, normalized by the tunnel dynamic pressure. As in the experiments (red dots), the peaks observed at 180 and 360 deg (FENSAP numerical solution in blue) correspond to passage of the rotor blades over station 2. The secondary peaks at around 22 and 202 deg., caused by passage of the blade tip vortex, have also been captured by this unsteady inviscid calculation.

Figure 9 presents time variation of the axial (fuselage longitudinal) velocity on the $Y = 0$ cutting plane (i.e., perpendicular to the rotor plane and located along the airframe centerline). Flow recirculation within a tip vortex is shown by positive (red) and negative (blue) axial velocity components. A first vortex is generated upstream of the rotation axis when the blade tip crosses the cutting plane. At the same time, a second vortex is generated downstream of the rotation axis by passage of the other blade tip. Other vortices, generated during previous rotations, can also be observed downstream of the rotor. All these vortices propagate in both downwash ($-Z$) and axial ($+X$) directions, interacting in time with the airframe.

Figures 10 and 11 present unsteady axial and downwash velocities at measuring station $X/R = 0.2$. As in the experiments, sharp dips in axial velocity correspond to passage of the tip vortex. In Fig. 10, the axial velocity changes from a value essentially close to freestream (10 m/s) to approximately stagnation conditions at about 112 deg. (compared with 117 deg. in the experiment) when the vortex is directly above it. At this instant (117 deg., exactly as in the experiment), the vertical velocity becomes negative (see Fig. 11). Both figures indicate, however, a small error in the position of the minimum axial velocity, and a larger predicted downwash velocity. This is explained by the inviscid assumption and the resulting lack of fidelity in predicting the structure of tip vortices.

B. Unsteady Impingement

Figure 12 presents three successive snapshots at different times of the unsteady liquid water content (LWC), each on three cutting planes along the axial direction. It can be observed that passage of the rotor generates a shadow zone (in blue) on the upper surface of the blade and aft. Furthermore, tip vortices induce recirculation in the drop velocity field (referred to as drop vortices in the text), leading to

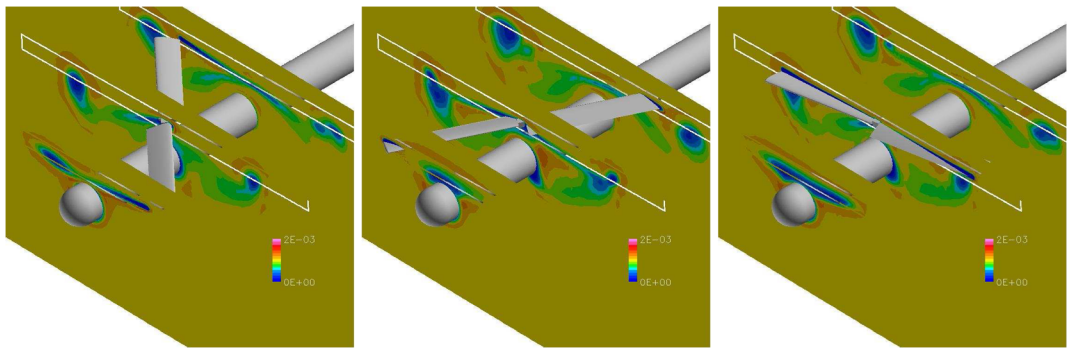

Fig. 12 Unsteady LWC on three cutting planes along the axial direction, and at three snapshots in time.

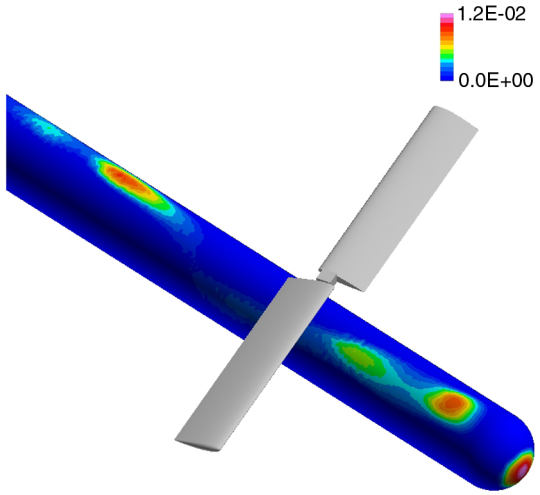

Fig. 13 Collection efficiency on the fuselage at a given instant in time.

pockets of low water content also shown in blue. These are dry regions caused by the centrifugal effect of air vortex structures expelling drops from their core. Their outer rim contains recirculating drops that, due to the centrifugal effect, lead to an enrichment layer (which can also be observed in Fig. 12). As for tip vortices present in the air solution, drop vortices are slowly shed downward due to the small advance ratio. The drop vortex structure is also affected by passage of the next rotor blade that cuts it in two and pushes it further downward.

This unsteady interaction and the downward direction of drop vortices generate impingement on the airframe below and downstream of the rotor. This is illustrated in Fig. 13 with the collection efficiency (nondimensional mass flow) on the airframe at a given instant in time. The spot on the nose of the airframe is due to forward motion and would be captured in a steady-state analysis. The four other spots correspond to different drop tip vortices impinging on the airframe.

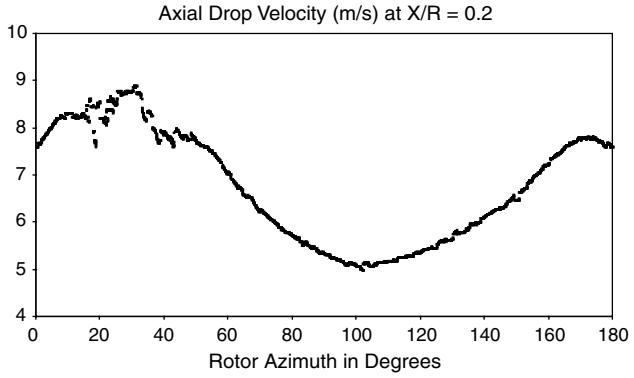

Fig. 14 Axial drop velocity (m/s) at $X/R = 0.2$.

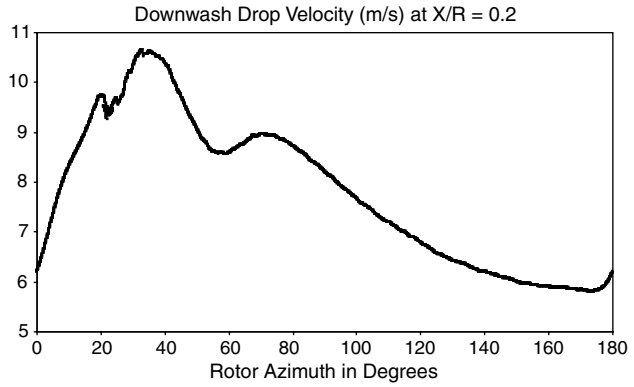

Fig. 15 Downwash drop velocity (m/s) at $X/R = 0.2$.

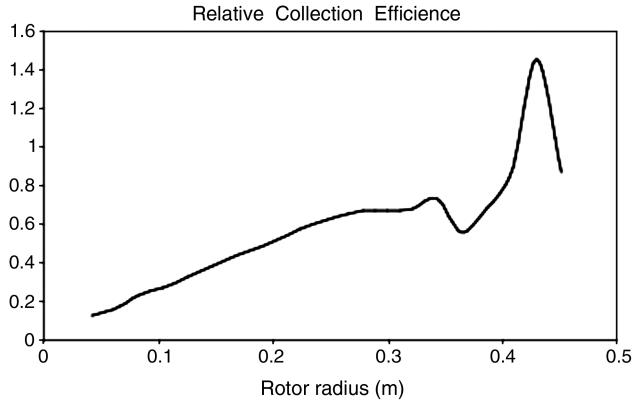

Fig. 16 Relative collection efficiency on the rotor as a function of radius (m), at an instant in time.

Figures 14 and 15 present the axial and downwash velocity components of water drops at measuring station $X/R = 0.2$. These should be compared with the air solution shown in Figs. 10 and 11. As for air, dips in axial drop velocity correspond to passage of the tip vortex. The minimum axial drop velocity is, however, nonzero (roughly 5 m/s) and positioned at 105 deg. instead of 112 deg. for air. Furthermore, the drop downwash velocity varies from 5.5 to -2 m/s, a lower range than for the air. These differences are due to the drop's higher inertia, and thus to a different structure and propagation speed of the vortices.

The major advantage of FENSAP-ICE-Unsteady for rotor simulation lies in its ability to capture impingement on moving bodies. This is shown in Fig. 16 with the relative collection efficiency (computed from the relative drop velocity) on the rotor leading edge at one instant in time. Most of the impingement occurs on the blade tip compared with the root. At this instant in time, the impingement pattern is also affected by interaction of the rotor leading edge with the drop tip vortex previously generated by passage of the other blade. This vortex of low LWC in its core, but of larger LWC on its rim, locally affects the predicted collection efficiency, as observed from a radius of 0.3 m to the tip.

C. Ice Location and Accretion Rate

Solving for 1 min of ice accretion at this rotor speed requires 2100 full rotations, which cannot be achieved in this work due to excessive solution time. The proposed strategy consists in computing ice rate and location (accumulated ice in time) over only one full rotation, and to assume that ice growth in time is then a multiplication of the initial

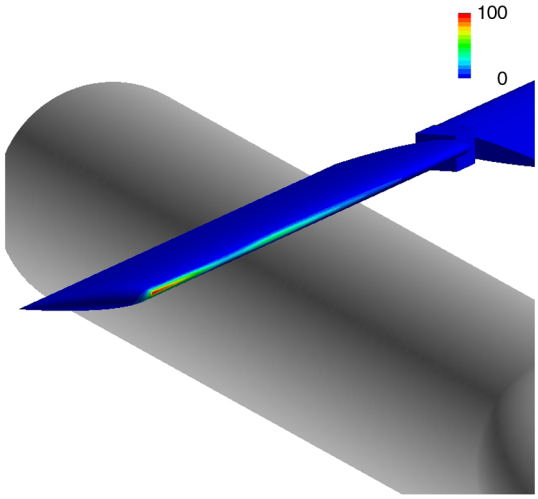

Fig. 17 Ice accumulation (in %) on the rotor after one full rotation. The airframe is shown in gray.

ice thickness. This corresponds to a quasi-steady ice accretion approach where the impact of ice growth on the flow and drop fields is neglected.

Since rime ice is considered, ice location is directly proportional to the relative collection efficiency, and thus to the unsteady LWC and drop velocity fields. Figure 17 presents normalized ice accumulation with respect to its maximum value (in %) on the rotor after one full rotation. Ice accretes mainly on the rotor tip due to the small advance ratio, and consequently, to the higher relative collection efficiency. Only traces of ice (below 0.01%) are observed on the airframe, in regions of drop vortices impingement and on the nose.

VIII. Conclusions

FENSAP-ICE-Unsteady attempts to truly represent the unsteady ice accretion phenomenon by using a multiphase unsteady in-flight icing model. The solver fully couples in time a two-phase flow (interacting air and droplet particles) with an ice accretion model. Numerical results show that, for rime icing conditions, the unsteady model improves the accuracy of ice prediction when compared with one-shot ice accretion. The latter predicted a bigger ice thickness on the upper surface of the wing (Fig. 3). Moreover, the dual time stepping approach largely reduces the computational time, making this new approach more appealing for industrial applications. Also, successful ice accretion simulation could only be achieved with smoothing techniques that effectively prevented wall elements distortion, and thus ensured good solver convergence.

The applicability of the icing model for predicting rime and glaze ice accretion was also demonstrated on stationary components and impingement results were obtained on a two-blade rotor and a generic cylindrical airframe. The unsteady flow and drop equations were solved in time with ALE terms that take into account rotation and ice accretion. This model was applied to rotor/fuselage flows by considering two grid domains: the first being fixed around the fuselage, and the second rotating with the blades. The gap between grid domains was stitched with elements to fully guarantee flow conservation.

FENSAP-ICE-Unsteady couples in time the air and drop equations for computing rotor-fuselage effects on LWC and drop velocities. Drop vortices interacted in time with the rotor and airframe, yielding impingement on the airframe below and downstream of the rotor, as well as unsteady variations of the collection efficiency on the rotor. Rime ice accretion was considered by coupling at each time step the flow and water drop equations to the Messinger icing model. The calculation performed over one full rotation (quasi-steady approach) showed that rime ice accreted mainly on the rotor tip. Traces of ice were, however, observed on the airframe due to the interactions of drop vortices with the generic cylinder.

Besides eliminating the arbitrariness of multishot ice accretion, the approach paves the way to a unified methodology of solving icing problems related to jet airplanes, turboprops, helicopters and engines. In addition, this would be done in an integrated way, i.e., as a system (airplane + propellers, helicopter + rotors, airplane+ jetengine), and not by reducing dimensions (airfoil sections rather than wing) or isolating components (rotor alone for example). The methodology ought to prove an able recipient of any new, empirical, or analytical, ice surface roughness data that varies in both space and time [21].

Acknowledgments

The authors would like to thank the Natural Sciences and Engineering Research Council of Canada and Newmerical Technologies International for sponsoring the development of this new icing model under an Industrial Postgraduate Scholarship program for the first author. They would like to thank Bell Helicopter Textron, Inc., for sponsoring the development and validation of the unsteady flow rotor-fuselage model in FENSAP.

References

[1] Bidwell, C. S., and Potapczuk, M. G., "Users Manual for the NASA Lewice Three-Dimensional Ice Accretion Code (LEWICE3D)," NASA TM 105974, 1993.

[2] Hedde, T., and Guffond, D., "ONERA Three-Dimensional Icing Model," *AIAA Journal*, Vol. 33, No. 6, June 1995, pp. 1038–1045. doi:10.2514/3.12795

[3] Bourgault, Y., Beaugendre, H., and Habashi, W. G., "Development of a Shallow-Water Icing Model in FENSAP-ICE," *Journal of Aircraft*, Vol. 37, No. 4, 2000, pp. 640–646.

[4] Togami, K., Tsujita, M., Aubé, M. S., and Habashi, W. G., "Validation Results of FENSAP-ICE," *Aircraft and Engine Icing International Conference*, SAE, Paper 07ICE-56, Sept. 2007.

[5] Beaugendre, H., "A PDE-Based 3D Approach to In-Flight Ice Accretion," Ph.D. Thesis, McGill Univ., Montreal, June 2003.

[6] Matheis, B. D., Huebsch, W. W., and Rothmayer, A. P., "Separation and Unsteady Vortex Shedding from Leading Edge Surface Roughness," *Enhancement of NATO Military Flight Vehicle Performance by Management of Interacting Boundary Layer Transition and Separation*, AVT-111, NATO, Prague, Oct. 2004.

[7] Mirzaei, M., Ardekani, M. A., and Doosttalab, M., "Numerical and Experimental Study of Flow Field Characteristics of an Iced Airfoil," *Aerospace Science and Technology*, Vol. 13, No. 6, Sept. 2009, pp. 267–276. doi:10.1016/j.ast.2009.05.002

[8] Kreeger, R. E., and Wright, W. B., "The Influence of Viscous Effects on Ice Accretion Prediction and Airfoil Performance Predictions," *43rd Aerospace Sciences Meeting and Exhibit*, AIAA Paper 2005-1373, 2005.

[9] Bragg, M. B., Broeren, A. P., Addy, H. E., Potapczuk, M. G., Guffond, D., and Montreuil, E., "Airfoil Ice-Accretion Aerodynamics Simulation," *45th Aerospace Sciences Meeting and Exhibit*, AIAA Paper 2007-0085, 2007.

[10] Mason, J. G., Strapp, J. W., and Chow, P., "The ice Particle threat to engines in Flight," *44th AIAA Aerospace Sciences Meeting and Exhibit*, AIAA Paper 2006-206, 2006.

[11] Alonso, J., and Jameson, A., "Fully-Implicit Time-Marching Aeroelastic Solutions," AIAA Paper 1994-0056, 1994.

[12] Aliaga, C. N., "An Unsteady Multiphase Approach to In-Flight Icing," Master Thesis, McGill Univ., Montreal, Feb. 2008.

[13] Hirt, C. W., Amsden, A. A., and Cook, J. L., "An Arbitrary Lagrangian–Eulerian Computing Method for All Flow Speeds," *Journal of Computational Physics*, Vol. 135, No. 2, Aug. 1997, pp. 203–216. doi:10.1006/jcph.1997.5702

[14] Oliker, L., Biswas, R., and Gabow, H., "Parallel Tetrahedral Mesh Adaptation with Dynamic Load Balancing," *Parallel Computing*, Vol. 26, No. 12, 2000, pp. 1583–1608. doi:10.1016/S0167-8191(00)00047-8

[15] Löhner, R., "Three-Dimensional Fluid-Structure Interaction Using Finite Element Solver and Adaptive Remeshing," *Computing Systems in Engineering*, Vol. 1, Nos. 2–4, 1990, pp. 257–272. doi:10.1016/0956-0521(90)90012-A

[16] Lepage, C., and Habashi, W. G., "Fluid-Structure Interactions Using the ALE Formulation," AIAA Paper 99-0660, 1999.

[17] Liou, S. G., Komerath, N. M., and McMahon, H. M., "Velocity Measurements of Airframe Effects on a Rotor in Low-Speed Forward Flight," *Journal of Aircraft*, Vol. 26, No. 12, April 1989, pp. 1131–1136. doi:10.2514/3.56816

[18] Liou, S. G., Komerath, N. M., and McMahon, H. M., "Measurement of the Interaction between a Rotor Tip Vortex and a Cylinder," *AIAA Journal*, Vol. 28, No. 6, June 1990, pp. 975–981. doi:10.2514/3.25153

[19] Liou, S. G., Komerath, N. M., and McMahon, H. M. "Velocity Field of a Cylinder in the Wake of a Rotor in Forward Flight," *Journal of Aircraft*, Vol. 27, No. 9, Sept. 1990, pp. 804–809.

[20] Mavris, D. N., Komerath, N. M., and McMahon, H. M., "Prediction of Aerodynamic Rotor-Airframe Interactions in Forward Flight," *Journal of the American Helicopter Society*, Vol. 34, No. 4, Oct. 1989, pp. 37–46.

[21] Croce, G., De Candido, E., Habashi, W. G., Munzar, J., Aubé, M. S., Baruzzi, G. S., and Aliaga, C., "FENSAP-ICE: Aanalytical Model for Spatial and Temporal Evolution of In-flight Icing Roughness," *Journal of Aircraft*, Vol. 47, No. 4, July–Aug. 2010, pp. 1283–1289.